PROCEEDINGS, 47th Workshop on Geothermal Reservoir Engineering
Stanford University, Stanford, California, February 7-9, 2022
SGP-TR-223

Hydraulic Transport Properties of Calcite Bearing Faults with Customized Roughness: Revisiting Hydro-Shear Stimulation Techniques

Mateo Acosta[1,2], Robin Maye[1,3] and Marie Violay[1]

1. École Polytechnique Fédérale de Lausanne; 2. now at California Institute of Technology; 3. now at KFSA Lausanne

mateo.acosta@epfl.ch

Keywords: Hydro-shear stimulation, Fracture fluid flow, Hydro-mechanical coupling

ABSTRACT

Understanding fluid flow in rough fractures is of high importance to large scale geologic processes and to most anthropogenic geo-energy activities. Here, we present the work conducted by Acosta et al. (2020) regarding fluid transport experiments on Carrara marble fractures with a novel customized surface topography. Transmissivity (fracture permeability) measurements were conducted under normal stresses from 20 to 50 MPa and shear stresses from 0 to 30 MPa. An open-source numerical procedure was developed to simulate normal contact and fluid flow through fractures with complex geometries. It was validated towards experiments. Using it, we isolated the effects of roughness parameters on fracture fluid flow. Under normal loading, we find that i) the transmissivity decreases with normal loading and is strongly dependent on fault surface geometry ii) the standard deviation of heights (h_{rms}) and macroscopic wavelength of the surface asperities control fracture transmissivity. Transmissivity evolution is non-monotonic, with more than 4 orders of magnitude difference for small variations of macroscopic wavelength and roughness. Experiments show that reversible elastic shear loading has little effect on transmissivity, it can increase or decrease depending on contact geometry and overall stress state on the fault. Irreversible shear displacement (up to 1 mm offset) slightly decreases transmissivity and its variation with irreversible shear displacements can be predicted numerically and geometrically at low normal stress only. Finally, irreversible changes in surface roughness (plasticity and wear) due to shear displacement result in a permanent decrease of transmissivity when decreasing differential stress. Generally, reduction of a carbonate fault's effective stress significantly increases its transmissivity while inducing small shear displacements doesn't. This highlights the need to reassess the hydro-shear stimulation technique in geo-energy activities, issue that is thoroughly discussed in this conference paper.

1. INTRODUCTION

The brittle-crust is pervasively fractured. Fractures seem to control most of the mechanical and hydraulic behavior of the upper crust, essentially at depths larger than 2-3 km (Townend and Zoback, 2000; Faulkner et al., 2010), where many anthropogenic geo-energy activities (geothermal power production, carbon capture and storage, nuclear waste repositories, etc…) take place. There, usual fracture permeabilites (10^{-18} to 10^{-16} m2) are 100-1000 larger than those of intact rock cores (10^{-21} to 10^{-19} m^2, Townend and Zoback, 2000). In deep geothermal power production, a popular strategy for enhancing fluid flow is hydro-shearing: injecting pressurized fluids to reactivate reservoir faults hoping to achieve permanent increases of permeability (Cladouhos et al., 2010; Breede et al., 2013, Cornet, 2016). The poor capacity to estimate long term flow rates are due to 1) imaging fracture networks in the underground, and 2) estimating fluid flow in rough, stressed fractures.

Fluid transport through a rough crack can be estimated through evaluation of its transmissivity (kt in m^3) e.g. the fracture's permeability (k in m^2) multiplied by the effective thickness (t in m) of the flowing fluid layer. Permeability thus corresponds to the transmissivity of a 1 m thick layer of flowing fluid (Rutter and Mecklenburgh, 2018). t depends on the porous space created between the contacting fracture's half-surfaces (Zimmermann and Bodvarsson, 1996).

Natural rock fractures usually present self-similar roughness (Brown and Scholz, 1985; Power et al., 1987; Brown, 1987; Candela et al., 2009; 2012; Renard et al., 2013), which, when in contact, generate a complex three-dimensional porous space through which fluids flow. The geometrical aperture distributions depend on the surface's geometries, and applied stresses (Zimmerman and Bodvarsson, 1996). A result of complex geometrical aperture distributions, flow channeling appears in fractures submitted to high stresses (Watanabe et al., 2009; Kang et al., 2016; Sawayama et al., 2021), drastically affecting the equivalent hydraulic aperture and transport capacity. Normal stress usually increases the amount of contact in the fracture, reducing the geometrical and equivalent hydraulic apertures (thus transmissivity; Witherspoon et al., 1980; Walsh, 1981; Renshaw, 1995; Brown 1987; Brown et al., 1998; Pyrak-Nolte and Morris, 2000; Watanabe et al., 2008; 2009; Kang et al., 2016; Rutter and Mecklenburgh, 2017; 2018). Reversible (elastic) shear stress application has rarely been studied experimentally but overall, it slightly decreases transmissivity (in smooth fractures of hard rock; Faoro et al., 2009; Rutter and Mecklenburgh, 2017; 2018). Experiments reproducing irreversible shear displacements (more than 1-20 millimeters) under low normal stresses (usually lower than 20 MPa; Carey et al., 2015; Ishibashi et al., 2012; Lee and Cho, 2002; Yeo et al., 1998; Pyrak-Nolte et al., 1988; Olsson and Brown, 1993; Esaki et al., 1999; Wenning et al., 2019; Chen et al., 2000; Watanabe et al., 2008; 2009) have convinced the community that shear displacement increases a fault's transmissivity. Such knowledge led generations of engineers to design hydro-shear stimulations in deep geothermal reservoirs which have mostly been failures. A few recent studies (Rutter and Mecklenburgh, 2017; 2018, Acosta et al., 2020) showed that small shear displacements (> 1 mm) reproduced under high normal stress (up to 100 MPa), result in a decrease of transmissivity or no increase at all. Such experiments can better be applied to hydro-shear stimulations since, if large displacements are generated, the risk of large magnitude seismicity increases (Zoback and Gorelick, 2017).

Here, we present most of the results of Acosta et al. (2020) where: 1) We developed an experimental technique to customize the roughness of hard-rock fracture surfaces. 2) We measured the wavy-rough fractures' transmissivity experimentally under normal stress (up to 50 MPa), under reversible shear stresses (up to 30 MPa), and under shear displacements (up to 1 mm total offset). 3) We developed an open-source numerical procedure simulating i) normal contact between wavy-rough surfaces ii) fluid flow through the resulting geometrical apertures. The procedure reproduced well experimental results and was therefore used to study the effects of roughness parameters on fracture transmissivity under normal load. We discuss the implications of our experimental and numerical results with respect to the hydro-shear stimulation technique and propose possible improvements in stimulation procedures of fractured deep reservoirs.

2. EXPERIMENTAL METHODS

Here, we detail the essentials of the experimental methods for comprehension of the conference paper. For detailed explanation of the methods, materials, and additional information, the reader is referred to Acosta et al. (2020).

2.1 Starting samples and surface roughness customization

Starting samples were ground-truth, saw-cut cylinders (75 mm length, 36 mm diameter, 30° angle fracture toward the long axis) of Carrara marble. For normal stress experiments, the saw-cut was along the cylinder's long axis allowing direct fluid flow through the fracture. For shear stress and displacement experiments, the saw-cut was at a 30° angle toward the long axis, and a borehole was drilled between the fracture surface and the cylinders' ends to allow fluid flow only through the fracture (Figure 1a and 1b).

To impose a customized roughness, the fracture's surfaces were set perfectly horizontal and were milled using a vertical-axis milling machine (Figure 1d). The rotary cutter was lowered into the surface and horizontally displaced at a given velocity. Depending on the rotation and displacement velocities, arc-shaped grooves were carved in the rock's surfaces with given wavelengths and direction of the grooves toward the fracture's long axes. Four different experimental geometries were used for this study (Figure 1c). The samples nomenclatures subscripts correspond to small (S) or large (L) wavelengths and direction with respect to fluid flow (P for sub-parallel and O for sub-orthogonal). Thus, M_{LO} corresponds to large wavelength with grooves sub-orthogonal to the sense of flow. M_{SO} corresponds to small wavelength with grooves sub-orthogonal to the sense of flow, and M_{LP} corresponds to large wavelength with grooves sub-parallel to the sense of flow. Finally sample with no customized roughness was used as control sample (M_f) where the roughness was imposed homogeneously grinding the sample with #80 grit (maps of the surface topographies are given in Figure 6).

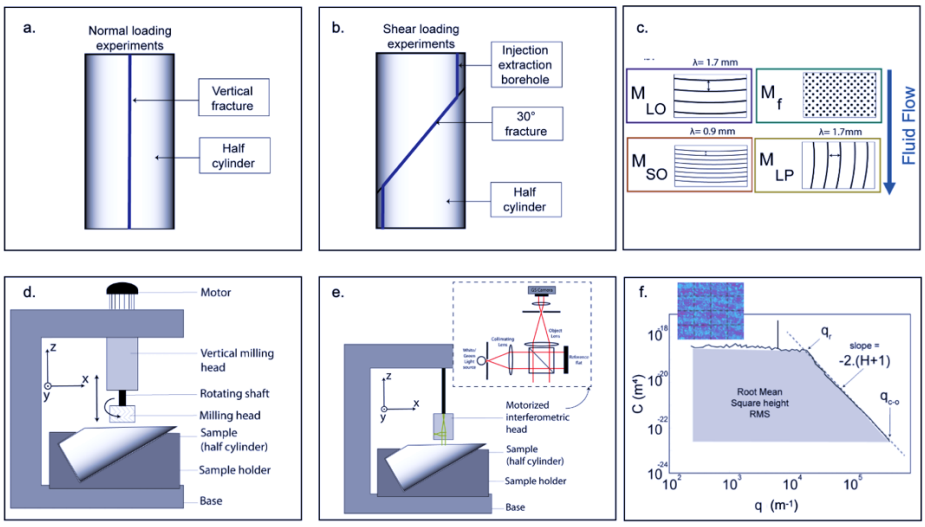

Figure 1: Experimental sample preparation and roughness customization. a. vertically saw-cut cylinders for normal stress experiments. b. 30° saw-cut cylinders with injection boreholes for shear experiments. c. sketches of the 4 surface roughness configurations. The used color scheme is maintained over the rest of the manuscript. d. diagram of the vertical axis milling machine for roughness customization. e. diagram of the profilometer used for roughness measurement. In d, and e., the bottom holder is motorized for displacement in the horizontal plane. f. example of a power spectral density of heights depicting a rough surface (example topography map in inset). For details refer to the experimental methods section and to Acosta et al. (2020).

The surface's roughness was measured through a 3D green light interferometer (profilometer) which has an accuracy of ~100 nm in height (Figure 1e). A stitching procedure allowed scanning large areas of the surface (10x10 mm, Figure 1f inset) to get a representative surface roughness measurement. The surface roughness statistics were evaluated through the radially averaged power spectral density of heights (PSD, Figure 1f). Some corrections to the raw measurement were performed following Jacobs et al. (2017) and are detailed in Acosta et al. (2020). The PSD allowed extraction of several roughness parameters: 1) the root mean square of heights (h_{RMS}, e.g., the area under the PSD vs wavevector curve); 2) the roll-off wavevector (q_r, e.g., the lowest wavevector where the PSD becomes a power-law (self-similar));), 3) the Hurst exponent (H, e.g. the characteristic value for the power law decay such that the power can be expressed as -2(H+1), for

details see Candela et al., 2012; Jacobs et al., 2017; Acosta et al., 2020); and 4) the characteristic wavevector (transformed to wavelength which represents a singularity in the PSD curve).

2.2 Experimental set-ups and procedure for flow through experiments

We used an oil-medium conventional tri-axial Hoek-cell to confine the reconstituted cylindrical samples and perform the flow through experiments (Figure 2a) with help of top and bottom volume-pressure controllers. For details of the setup, the reader is referred to Noel et al., 2019, Orellana et al., 2019; or Acosta et al., 2020).

2.2.1 Normal stress flow through experiments

The vertically saw-cut saturated samples were confined to the target confining pressure of 43 MPa, and the mean pore fluid pressure was varied stepwise to modify the effective normal stress on the vertical saw-cut which ranged from 28 to 40 MPa. At every step, a differential pressure of 0.3 MPa was imposed between the top and bottom pressure controllers to establish a constant flow rate which was measured through the fracture (Figure 2b). The transmissivity of the fracture was determined using Darcy's law as (Rutter and Mecklenburgh, 2018):

$$kt = \mu . \frac{Q}{w . \left(\frac{\Delta p_f}{L}\right)} \tag{1}$$

Where μ is the dynamic viscosity of the fluid, Q is the steady state flow rate, w the fracture's width, L its length, and Δp_f the differential pressure imposed.

2.2.2 Shear stress and displacement flow through experiments

The 30° saw-cut saturated samples were confined to either 15 or 35 MPa for low stress and high stress experiments. This time, the mean pore pressure was set to 5 or 15 MPa respectively to have effective confinements of 10 and 20 MPa. Then, the axial displacement was increased stepwise (0.1 mm per step) at constant displacement rates of 10^{-6} mm.s^{-1} to allow fluid pressure-volume equilibrium in the samples during shearing (Figure 2c). Under this saw-cut configuration, the stresses on the fault were calculated as:

$$\tau = \frac{(\sigma_1' - \sigma_3')}{2} \sin(2\theta) \text{ , for shear stress, and} \tag{2}$$

$$\sigma'_N = \frac{(\sigma_1' + \sigma_3')}{2} - \frac{(\sigma_1' - \sigma_3')}{2} \cos(2\theta) \text{ , for normal stress} \tag{3}$$

with σ_1' the effective axial stress on the sample, σ_3' the effective confinement, and θ the angle between the fracture and the vertical.

The total axial displacement after 10+ steps was usually of ~1.1mm, resulting in a final shear offset of ~1 mm (Figure 2c). After each displacement step, the axial piston was held in position for transmissivity measurement. After the natural relaxation of differential stress, a pore fluid pressure differential of 0.3 MPa was imposed to measure transmissivity under steady-state flow configuration. Under the elliptical fault geometry of shear experiments, the transmissivity can be expressed as:

$$kt = \frac{Q . \mu . \log_e \left(\frac{2a_e}{r_0} - 1\right)}{B . \pi . \Delta p_f} \tag{4}$$

with a_e the half distance between the injector and extractor boreholes, r_0 the borehole diameter, and B a constant close to unity. It is noteworthy that here we use Δp_f rather than $\frac{dp_f}{dx}$ as was wrongly written in Acosta et al. (2020) and Rutter and Mecklenburgh (2018). In Acosta et al. (2020) the calculations were correctly performed but the error in the written equation was kept in the final manuscript. For details on the correction for fluid flow through elliptical fractures using injection/extraction boreholes, the reader is referred to Ji et al. (2022).

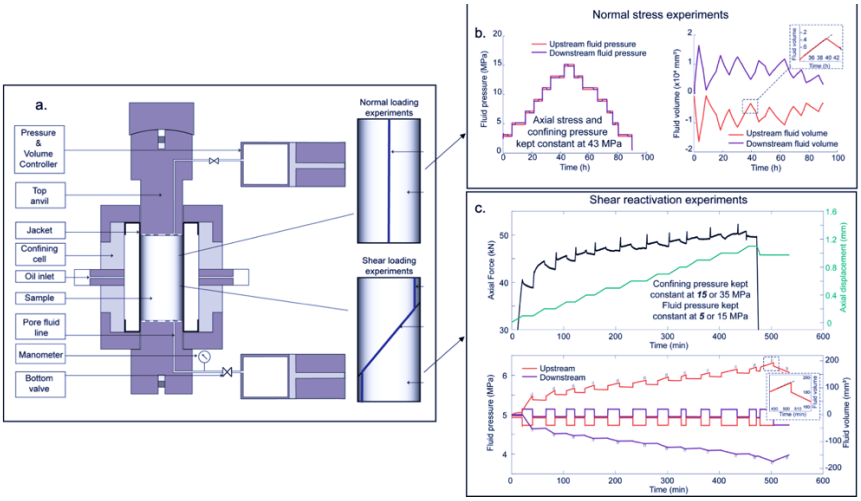

Figure 2: Experimental set-up and flow through experiments. a. The Hoek-cell tri-axial set-up with customized fluid pressure system for flow through experiments (After Noël et al., 2019). b. Example normal loading experiments. Axial stress and confining pressure were fixed at 43 MPa. The changes in mean fluid pressure led to a change in effective normal stress applied on the fracture. b, Left panel: Upstream and downstream fluid pressures versus time. b, Right panel: Upstream and downstream volumes versus time. The imposed differential pressure resulted in a symmetric volume rate at the pressure/volume controllers which was held until achieving a steady state. Inset shows zoom on one example of the flow rate versus time. c Example of shear loading experiments. c, Top panel: Axial force (black) and axial displacement (green) versus time. The increase in axial displacement led to a spontaneous evolution of the axial force (therefore of shear and normal stress) applied on the 30° saw-cut fracture. c, Bottom panel. Fluid pressures (left x-axis) and volumes (right y-axis) versus time. A differential pressure of 0.3 MPa was imposed at every displacement step to measure transmissivity in steady state. Insert shows a zoom on one example of the flow rate versus time. The example in panel c. is given for an experiment at 10 MPa effective confinement. Figure is modified from Acosta et al. (2020)

2.3 Numerical modelling of fracture transmissivity under normal stress

We model the transmissivity of a rough fracture submitted to normal stress by combining three open-source procedures as follows:

1) Generation of artificial rough surfaces:

The roughness parameters (h_{RMS}, H, q_r) from the measured initial surfaces' PSD's (Figure 1f; Figure 6e-g) are input into the algorithm of Kanafi (2019) which generates an artificial rough surface similar to the experimental one. On top of it, we manually add a macroscopic wavelength (singularity in the PSD) such that the roughness parameters are conserved (See Acosta et al., 2020; and Jacobs et al., 2017 for details). An example of the numerical wavy rough surface is given in Figure 3a and can be compared visually to figure 3d (the latter being a subset of the whole surface).

2) Simulation of normal contact:

We use the half-space based dry contact model from *Tribonet* (Lubrecht and Ioannides, 1991; Polonsky and Keer, 1999; Akchurin et al., 2015) which considers a double-continuum convolution integral to calculate the deflection of the contacts at each mesh node and its effect on all the surrounding nodes. Two rough surfaces are put in contact and the solid material is assigned an elastic-perfectly-plastic constitutive law (saturated elastic deformation) whose parameters were measured experimentally (See Acosta et al., 2020's annex for details). The material Young's modulus is taken as 30.2 GPa, its Poisson's ratio 0.3, and the yield stress as 0.2 GPa (saturation threshold, Violay et al., 2013). As a result, contact maps accounting for mechanical interactions between two rough surfaces are generated (Figure3b). As expected, with increasing applied normal stress, the contact distribution changes (overall the contacts grow and new contacts appear) and the real area of contact increases. This procedure generates a realistic distribution of contacts (or asperities) for a given normal stress, and thus realistic geometrical apertures in the rough fracture.

3) Simulation of fluid flow through the fracture:

To simulate fluid flow through the rough fracture (Figure 3c), we input the contact map (or rather the aperture map) into a finite volume formulation model that solves the Reynolds boundary layer approximation for fluid flow (simplified to the local cubic law; Crandall et al., 2017; Brush and Thompson, 2003; Reynolds, 1886). This model assumes that the variations in aperture are gradual (it holds because $\frac{h_{RMS}}{\lambda} \ll 1$ and $\frac{L}{\lambda}>10$, for details refer to Acosta et al., 2020) so that the boundary layer approximation can be written:

$$\int_s \rho.\left[\frac{e_m^3}{12.\mu}.\nabla p\right].\hat{n}.dS = 0$$

(5)

Where ρ is fluid density, $e_m(x,y)$ the local geometrical aperture, S the domain's surface, and $\hat{n}$ the outward unit vector to each local element. We use boundary conditions representative of the experimental problem.

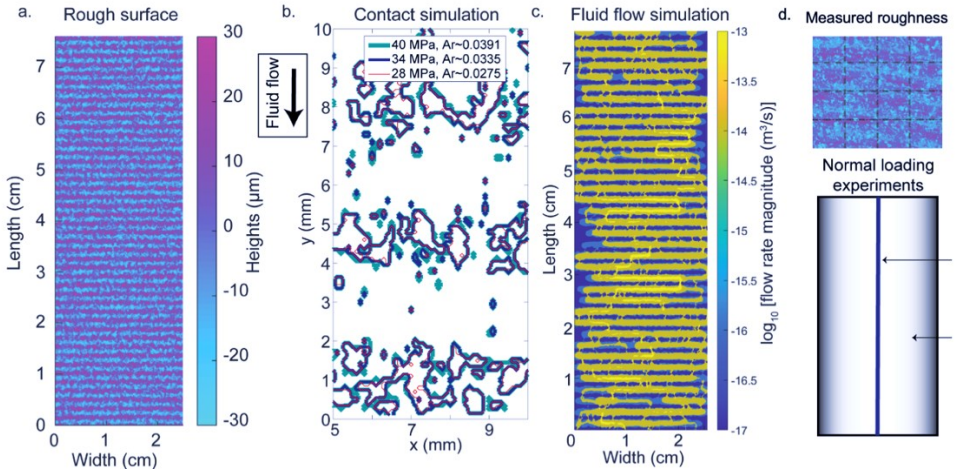

Figure 3: Numerical modelling of fluid flow through rough surfaces. a. Example of one artificially generated surface, colorbar accounts for the height distribution. b. results from normal contact simulations. Zoom on a 10 mm*5 mm part of the surface representing the contact area between two rough surfaces. Different contact areas under confining pressures are shown (28, 34, 40 MPa are respectively the thin red, blue, and thick turquoise contours) c. Example of a flow through simulation performed with the contact area at σ'_N =28 MPa as input. Colorbar shows the flow rate magnitude through the fracture in logarithmic scale. d. Example of the corresponding experimental surface map (same colorbar as a.) and sample configuration for the simulations (not to scale).

3. RESULTS

We present the results from Acosta et al. (2020). In each figure, a schematic legend shows the corresponding sample's roughness, with the directions of flow and shear that correspond to the experiment/numerical simulation. We first present the results of experiments and numerical simulations of normal loading set-up. Then, we present the results of shear loading experiments and the corresponding microstructures.

3.1 Normal stress experiments and numerical procedure

Figure 4a shows the results of normal stress experiments. Dashed lines represent a first run-in phase for sample transmissivity, and full lines represent the results considered in the analysis. It is noteworthy that in permeability/transmissivity measurements, the run-in cycle usually presents different results from further cycles (see Rutter and Mecklenburgh, 2017; 2018, and Acosta et al., 2020 for details). The experimental sample M_{LO} showed transmissivities ranging from 3.05e-18 m^3 at σ_3'=28 MPa down to 0.76 e-18 m^3 at σ_3'=40 MPa. Then, M_{SO} showed transmissivities half an order of magnitude smaller than those of M_{LO} (ranging from 0.49e-18 m^3 down to 0.17 e-18 m^3 at σ_3'=40 MPa). The sample with no imposed macroscopic wavelength, M_f had transmissivities ranging from 0.23e-18 m^3 down to 0.15 e-18 m^3. The transmissivities were close to those of M_{LO} and M_{SO} but the decay with increasing confinement was smaller in this experiment with respect to the samples with macroscopic wavelength. The sample M_{LP}, had transmissivities ranging from 0.48e-18 m^3 at σ_3'=28 MPa down to 0.20 e-18 m^3 at σ_3'=40 MPa. The transmissivities were almost half an order of magnitude lower than those of M_{LO} and close to those of M_{SO}.

Figure 4b shows the results of numerical transmissivity simulations for fully mated surfaces (circles) and fully un-mated surfaces (triangles). The simulations for fully mated surfaces are in strong compatibility with the experimental results within a factor of 2.5 (Figure 4c) whereas for un-mated surfaces, the numerical simulations overpredict transmissivity by ~3 orders of magnitude. The numerical results show that for mated surfaces, the initial roughness can strongly affect the exponential decay of transmissivity with effective stress (fits in figure 4b) but that overall, a decrease in effective stress of ~15 MPa can change the fracture's transport capacity by 1+ orders of magnitude. Note that the effective stress studied in this work remains high and this effect could be more intense at low stress values. The 2.5 factor of error between predicted/measured transmissivities probably exists because experimental samples are rarely in a fully mated configuration due to imperfections in the surfaces which disappear in the numerical procedure (which reproduces perfectly wavy rough surfaces, perfectly mated).

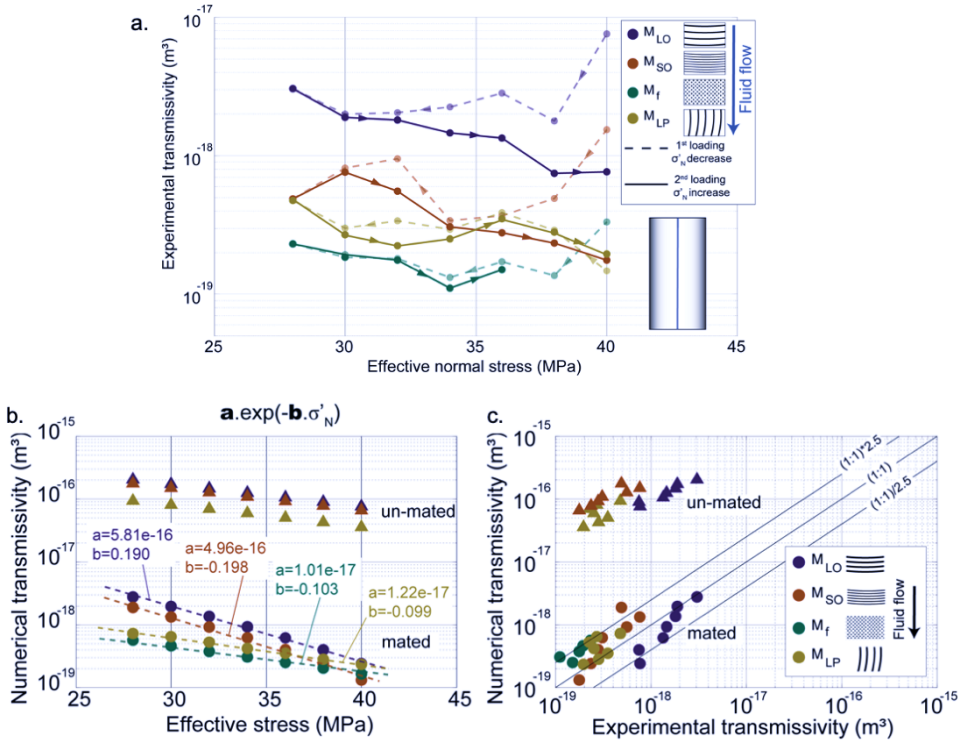

Figure 4: Experimental and numerical results of transmissivity versus effective normal stress. A. Experimental results for the 4 sample configurations. b. Numerical results, circles represent mated surfaces (fully imbricated) and triangles represent un-mated surfaces. c. Comparison of numerical and experimental transmissivities. When the surfaces are mated, the numerical procedure represents very well the experimental values within a factor of 2.5.

3.2 Shear stress experiments and microstructures

Figure 5 shows for each sample's roughness, the evolution of shear stress versus axial displacement (left y-axis, solid lines), and the evolution of transmissivity (right y-axis, dotted lines). In each panel, we show two experiments: one conducted at low effective confining pressure (10 MPa, lighter colors), and one conducted at high effective confining pressure (20 MPa darker colors).

In all experiments, we observe a decrease in transmissivity during elastic loading (steep part of the shear stress-displacement curve) of 1+ orders of magnitude. This seems reasonable since in our configuration, the normal stress also increases during this phase (See Acosta et al., 2020 for details). Then, once the fault starts sliding, the transmissivity either decreases or remains almost constant with no significant increase of transmissivity in any case (flat part of the shear stress-displacement curve). Finally, when stress was unloaded, transmissivity slightly increased (of ~0.1 orders of magnitude) but remained ~1 order of magnitude lower than before shear displacement at the same stress levels. It is noteworthy that at lower effective confinement (e.g. lower normal stress), transmissivity was 1 to 2 orders of magnitude larger than at higher stress for the initial measurement (no displacement, no differential stress), for the measurements at the end of elastic loading, during shear displacement and after unloading. These results will be discussed further in section 4.

Microstructures are presented in Figure 6. Surface topography maps of intact samples in Figure 6a1 to 6d1, of sheared samples for experiments conducted at $\boldsymbol{\sigma'_3}$= 10 MPa in Figure 6a2 to 6d2, and of sheared samples for experiments conducted at $\boldsymbol{\sigma'_3}$= 20 MPa in Figure 6a3 to 6d3. The radially averaged 2D PSD curves are given in Figure 6e, 6f, and 6g respectively for intact samples, sheared at 10 MPa effective confinement, and sheared at 20 MPa effective confinement.

The PSD's presented a first part where the power spectral density was close to constant with increasing wavenumber until the roll off wavevector q_r (Figure 1f and Figure 6e-g). There, the macroscopic wavelengths appeared as a peak (singularity) in the PSD curves. As the wavenumber increased past q_r, a second part having a power law dependence on wavenumber could be characterized by the power $-2(H+1)$ with H the Hurst exponent (Candela et al., 2012; Jacobs et al., 2017). Finally, the area under the PSD curves represents the Root Mean Square of heights (h_{RMS}) which is the standard deviation of the heights distribution (Candela., 2012; Jacobs et al., 2017 and references therein). Prior to deformation, for $q< q_r$, the samples M_{LO} had PSD amplitudes ($C(q<q_r) \sim 2.10^{-19}$ m^4), and the samples M_{SO} and M_{LP} had smaller PSD amplitude prior to roll off ($C(q<q_r)$ ~7-8.10^{-20} m^4). Finally, the sample with no macroscopic wavelength -M_{f}- had the smallest PSD amplitudes prior to roll-off ($C(q<q_r)$ ~1.10^{-20} m^4). The roll of wavenumbers were the smallest for M_{LO}, M_{LP} and M_{SO} (q_r~6900 rad.m^{-1}). q_r were larger for the sample with no macroscopic wavelength M_{f} (q_r~10000 rad.m^{-1}). Regarding Hurst exponents determined from the slope of the PSD curves, the samples M_{LO} and M_{SO} had H respectively 0.47 and 0.60. The sample with no macroscopic wavelength M_{f} had lower H~0.44 and finally M_{LP} had H~0.59. The largest h_{RMS} were calculated for M_{LO} and M_{SO} (~9.0 and 8.0 μm respectively). Then, M_{f} had lower h_{RMS} ~4.5 μm and finally M_{LP} had h_{RMS}~7.5 μm. The sample M_{LO} had a macroscopic

wavelength λ= 1.7 mm with while the M_{SO} surfaces had λ= 0.9 mm. Both samples had an imposed wavelength amplitude of 11 μm. Finally, M_{LP} had λ= 1.7 mm with an amplitude of ~9 μm (fore details go to Acosta et al., 2020).

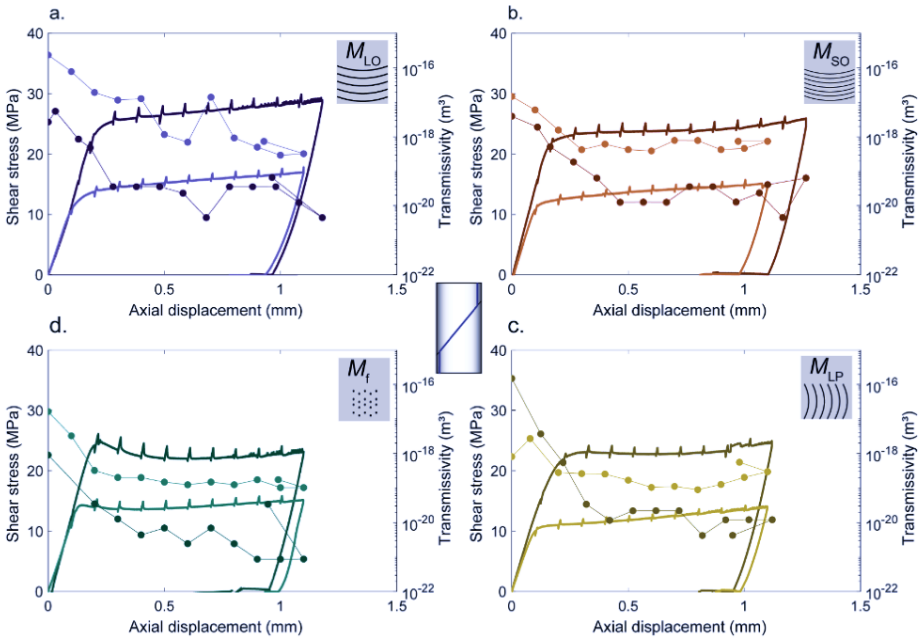

Figure 5: Coupled evolution of fault's shear stress, and transmissivity in response to axial loading. In all panels, left y-axis shows shear stress right y-axis shows fault's transmissivity (circles) and x-axis is the axial displacement. Note that the shape of normal stress evolution is like that of shear stress, so shear displacement occurs at relatively constant normal stress (see Acosta et al., figure 4 for details). Darker and lighter colors represent experiments conducted at 20 and 10 MPa effective confining pressure respectively. a. Experiments on sample M_{LO}. b. Experiments on sample M_{SO}. c. Experiments on sample M_f. d. Experiments on sample M_{LP}.

We observe that for sheared samples, the presence of a third body appears after the experiment. The surface topography strongly changes both due to the appearance of the third body (gouge) and shearing off of certain topography features. This effect becomes stronger with increasing confinement (compare lines 1, 2 and 3 of the topography maps). The amount of change is dependent on the initial surface roughness (compare line 3a to d of the topography maps). It appears visually in the topography maps as new grooves in the sense of shear. The change in surface topography manifests in the PSD as a decrease in the height of the singularity (macroscopic wavelength) as well as in the homogenization of the PSD curves. Indeed, the initial sample PSDs (Figure 6e) presented a bi-linear evolution with wavevector (at wavevector q_r, Figure 6e) which is less marked in sheared samples (Figure 6f, 6g). The PSDs present more and more self-affine features with shear.

4. DISCUSSION

4.1 The effects of normal stress and roughness on fracture transmissivity: reservoir preconditioning

We showed that the hydraulic transport properties of rough fractures are strongly controlled by the application of normal stress. The normal stress dependence of transmissivity depends on the surface geometries, the roughness parameters, and the imbrication of the fractures (largest features). This has been shown in Section 3; and some of these features were shown in in previous studies (Chen et al.2000; Watanabe et al., 2008; 2009; Patir and Cheng, 1978; Iwai, 1976; Pyrak-Nolte et al., 1988; Walsh, 1981; Witherspoon et al., 1980; Rutter and Mecklenburgh, 2017; 2018). The numerical results are remarkably consistent with the experimental data (more than 90% of the points are contained within a factor 2.5 from the experimental data) and thus, we can use the numerical procedure to explore the influence of different roughness parameters on the transmissivity of rough fractures (Figure 7a, and 7b). We systematically modified the roughness parameters for wavy rough surfaces (with a macroscopic wavelength, Figure 7a1 to 7a4). We observe that H and q_r have very little influence on transmissivity (Figures 7a 1 and 7a2) within reasonable values for natural and laboratory fractures (Candela et al., 2009; Acosta et al., 2020). Macroscopic wavelength (Figure 7a3) and h_{RMS} (Figure 7a4) have the largest influence both on transmissivity and on its exponential decay with increasing normal stress. We then explored the transmissivity values in this parameter space for a constant normal stress of 28 MPa (Figure 7b). Transmissivity has a non-monotonic dependence on these two parameters with more than 4 orders of magnitude difference in the parametric space. This result shows how important the roughness parameters are when trying to predict fluid flow through fractures.

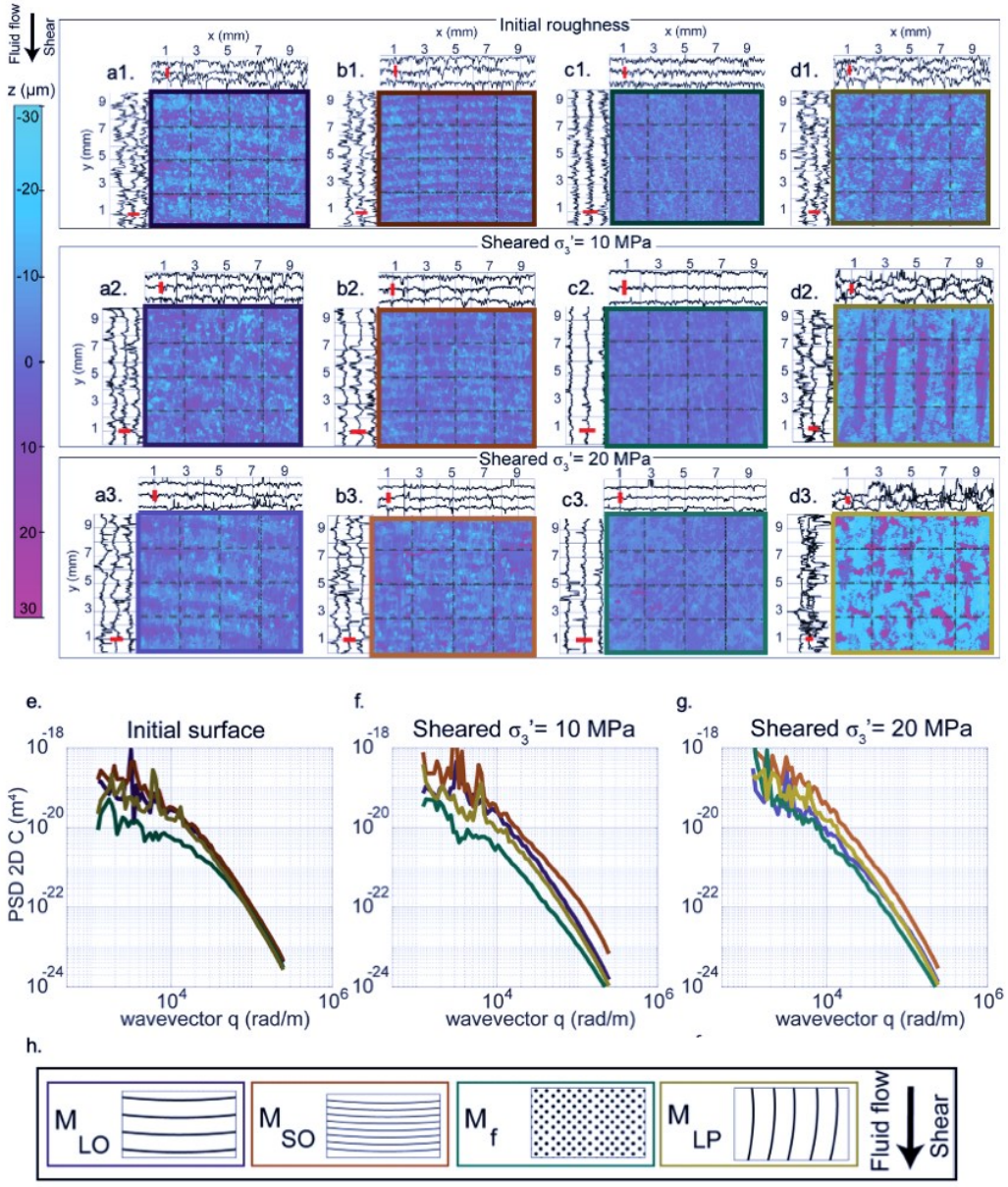

Figure 6: Microstructural and roughness analysis. a-d. Experimental surface topography maps. Colorbar represents the measured heights over the area. The transects in x-axis and y-axis in dotted lines are presented in the top and left plots respectively. For reference, a red bar represents 30 micrometer height. a1 to d1. Maps of surface roughness before deformation. a2 to d2. Post-deformation surfaces for experiments conducted at 10 MPa effective confinement. a3 to d3. Post-deformation surfaces for experiments conducted at 20 MPa effective confinement. First column represents samples M_{LO} (panels a1, a2, a3.); second column represents samples M_{SO} (panels b1, b2, b3); third column represents samples M_f (panels c1, c2, c3.); and fourth column represents samples M_{LP} (panels d1, d2, d3). Panels e, f, g. represent the measured radially averaged PSD's for rows 1 (initial rough surfaces), 2 (surfaces after shear deformation at 10 MPa effective confinement), and 3 (surfaces after shear deformation at 20 MPa effective confinement). Panel h. depicts a sketch of the surface geometries with the colors represented in all the other panels.

Because of the difficulty in estimating a fracture's roughness in natural geothermal (or other geo-energy reservoirs), we propose that one of the best paths to improve the reservoir's transport capacity is to somehow reduce the stress levels in the reservoir prior to the production phase and maintain low stress levels during it. This could be done either through two main strategies:

1) Long term hydraulic pre-conditioning: If several wells are drilled into the reservoir, slowly injecting fluids in all wells during preconditioning can help reduce the effective normal stress in the reservoir at rates that allow the rock fractures to equilibrate stresses to avoid large magnitude seismicity. Of course, much care must be taken not to reach the failure envelope of the optimally oriented fractures avoiding their reactivation, and potential induced seismicity. Then, once the reservoir reaches lower effective stress levels,

injection/production on the reservoir should be improved because fractures operate at much lower stress levels than under the initial conditions and their transmissivities could be increased. If we extrapolate values from our measurements to the problem in question, assuming the overall effective stress in the fractures decreases from 36 to 28 MPa due to pre-conditioning, their transmissivity could increase from ~2e-19 to 5.5e-19 m^3 in the worst roughness case scenario, or from ~6e-19 to 3e-18 m^3 in the best roughness case scenario. For an equivalent square fracture in the reservoir of size L=w, and with an imposed differential pressure between fracture's ends of 1 MPa, the fluid flow in that reservoir should increase from 0.22 to 0.61 e-6 $l.s^{-1}$ in the worst-case scenario or from 0.67 to 3.3 e-6 $l.s^{-1}$. A significant increase in fluid flow through the fracture can be achieved this way. The main inconvenient of this method is that even though the normal stress can be decreased by injecting pressurized fluids, the shear stress is not expected to decrease or at least not significantly. Therefore, the risks of seismicity remain high, even though productivity has indeed increased.

2) Thermal preconditioning: The details of reservoir thermal preconditioning can be found in Fryer et al. (2020). The main idea is to exploit the faulting regime's characteristics of stress orientation to inject fluids that will cool the reservoirs (or zones close-to the reservoir). This will generate thermal contraction/dilation in the reservoir such that the normal and shear stresses decrease in the reservoir prior to production (Figure 7b). Aside from the concept detailed in Fryer et al. (2020), it has been shown that stress depletion effect due to reservoir operations can be 60% hydraulic and 40% thermal in nature (Im et al., 2021) in the case of the Coso geothermal field. Such stress depletion resulted in a notable lack of aftershocks from the 2019 Ridgecrest earthquake within the area of the geothermal field. This effectively shows that, by preconditioning a reservoir, one can achieve lower levels of seismicity due to stress depletion. Considering our results, one should also expect higher transmissivities in the reservoir's fractures and so higher flow rates for production of geothermal fluids. Extrapolating our results and considering the 'preconditionment' results from Im et al. (2021), the flow rates could increase of more than 2 orders of magnitude in a set-up such as the Coso reservoir. The main drawback of this method is that cooling down the reservoir can result in lower power production due to the lower temperatures reached. Overall, an optimization of heat extraction could be done for a reservoir design.

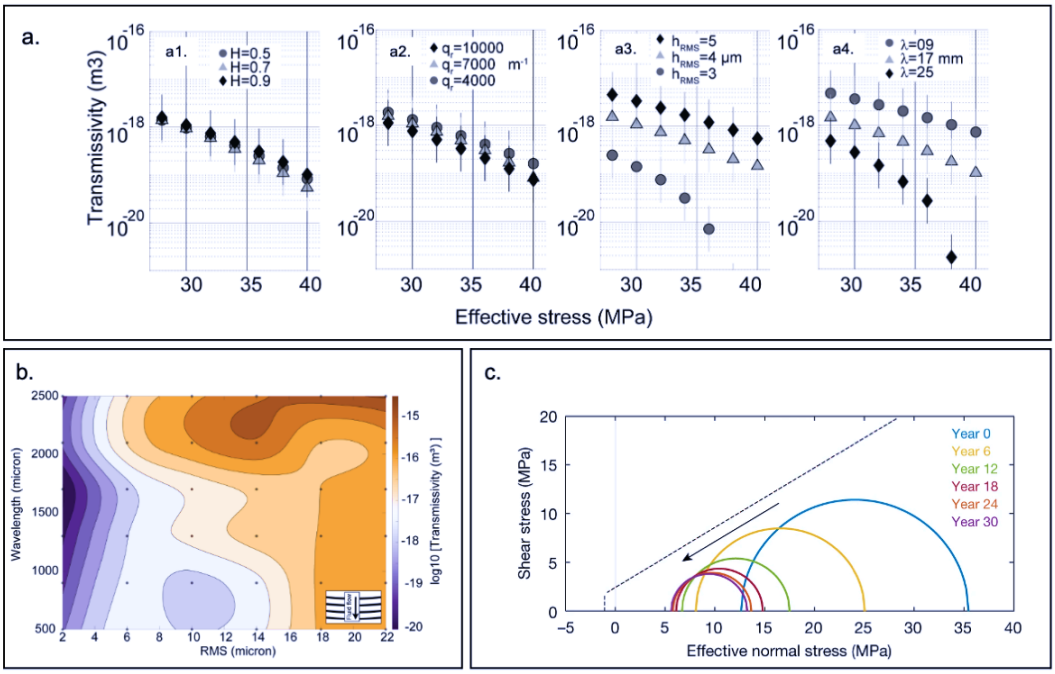

Figure 7: Parametric analysis of the influence of surface roughness on transmissivity and concept of reservoir preconditioning. a. Parametric analysis of transmissivity versus effective stress for 1) flat rough surfaces (no macroscopic wavelength, panels a1 to a3). 2) wavy-rough surfaces (with macroscopic wavelength, panels a4 to a7). Each panel represents the variation of a given roughness parameter. Overall, the macroscopic wavelength and root mean square roughness have the most control on transmissivity. b. Contour plot of transmissivity in rough wavy surfaces (grooves sub-orthogonal to fluid flow). The fault's transmissivity (in log scale) is computed as function of the root-mean-square roughness (h_{RMS}) and the macroscopic wavelength. Effective pressure considered for this plot is 28 MPa. The transmissivity is strongly non-monotonic with these two parameters. c. After Im et al. (2021). This panel illustrates the concept of reservoir preconditioning, it represents the evolution of normal and shear stress over 30 years of geothermal reservoir operations at the Coso geothermal field from numerical simulations. The fluid injection/extraction operations combined with the thermal cooling of the reservoir result in an overall decrease of the normal and shear stress applied on reservoir faults of more than 20 MPa in normal stress and 10 MPa in shear stress. As a result, the region was depleted of aftershocks following the 2019 Ridgecrest earthquake. Similar reservoir pre-conditioning concepts were proposed by Fryer et al. (2020).

4.2 The effects of shear stress and displacement on fracture transmissivity: efficiency of hydro-shear techniques

We showed that small shear displacements on rough fractures do not increase their transmissivity under any surface roughness configuration. This result (confirmed by the experiments of Rutter and Mecklenburgh, 2017; 2018; Faoro et al., 2009; Tanikawa et al.,

2010) is counter-intuitive towards the common knowledge regarding fracture reactivation in shear. Usually, hydro-shear stimulation techniques assume that shear slip on a fracture results in an increase of its hydraulic transport capacity due to shear induced dilatancy (for example see Cladouhos et al., 2010; Breede et al., 2013, Cornet, 2016; Ciardo and Lecampion, 2019; Carey et al., 2015; Guo et al., 2013; Ishibashi et al., 2012; Lee and Cho, 2002; Yeo et al., 1998; Zambrano et al., 2018; Pyrak-Nolte et al., 1988; Olsson and Brown, 1993; Esaki et al., 1999; Wenning et al., 2019). Most of these previous experimental studies induced very large shear displacements on fractures submitted to very low normal stress to observe the increase in transmissivity. In deep geothermal reservoirs, stimulations that generate large shear displacements are usually associated with the occurrence of large magnitude seismic events and thus need to be avoided. In addition, we expect that at deep reservoir depths, stresses are higher than 10 MPa in most cases.

In Figure 8a, we present a conceptual diagram of what could be occurring in our experiments with respect to the usual knowledge applied to hydraulic stimulations: At low normal stress, increasing shear stress will result in asperities riding past one another (Engelder and Scholz, 1976; Morad et al., 2022). For long enough displacements, this should result in a permanent increase of transmissivity due to geometrically induced shear dilatancy (Figure 8a top and bottom left panels). On the other hand, in our experiments, and in deep geo-eenergy reservoirs, the mechanism seems different: at high normal stress, creation of shear displacement is the result of asperities failing in shear (Figure 8a top and bottom right panels, Engelder and Scholz, 1976; Morad et al., 2022). This not only does not allow (or reduces) geometrically induced shear dilatancy but generates large amounts of gouge that block the hydraulic paths for fluid flow as was observed in our experiments (Figure 6, and section 3.2) and was very recently demonstrated experimentally on rough faults by Morad et al. (2022). Such mechanism at high stress (and small shear displacements) results in a stress-transmissivity evolution with shear displacement as the one observed in our experiments (Figure 8b). We can well imagine that, at high stresses, the hydro-shear stimulation efficiency is reduced compared to low stress conditions, another reason why the reservoir preconditioning technique can be useful.

Finally, some limitations of this study are: (1) it is noteworthy that our experiments simulate a young fracture with no pre-existing shear displacement, and no clogging. If the fractures are 'clogged' (due to the presence of frictional wear products or by mineral precipitation), it is highly possible that shear reactivation, followed by an unclogging treatment (chemical or hydraulic for example) does increase the fractures transmissivities (Elkhoury et al., 2011). This should be studied in future work and can lead to a new view on hydro-shear stimulations. (2) The experiments presented by Acosta et al. (2020) were run in calcite bearing samples. Calcite has a yield stress od ~200 MPa, meaning that asperity contacts will plastify under low nominal fracture normal stress. In the case of silicate-bearing rocks, the yield stress should be 10-50X larger thus, the evolution of the aperture field should be drastically different with increasing stress. The wear processes will also differ in silicate bearing rocks thus the flow channeling should differ with increasing shear displacement. This is the target of ongoing work.

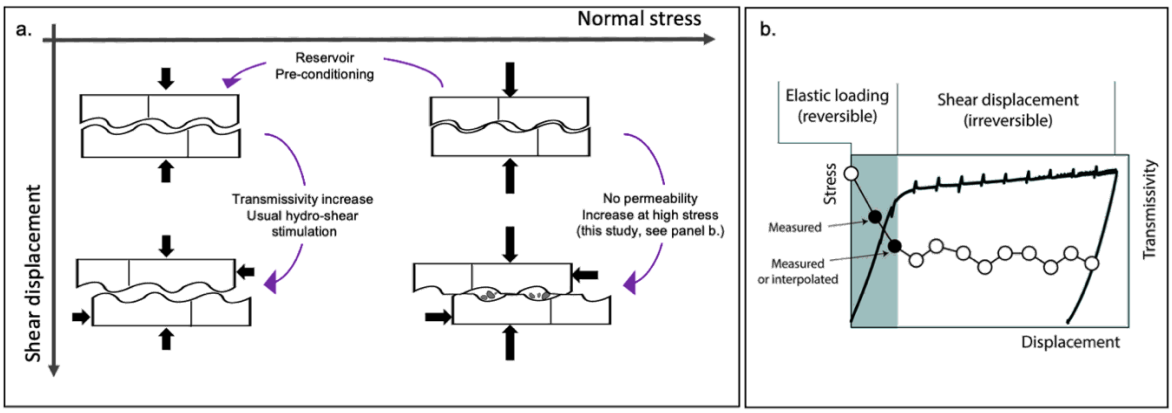

Figure 8: Conceptual diagram of the influence of normal stress and shear displacement on fracture's geometrical and hydraulic aperture. a. four different fracture contact states with increase of normal stress (left to right) and increasing shear displacement (top to bottom). The hydro-shear stimulation technique assumes that reactivation in shear leads to dilatancy and thus to increased transmissivity. This could be true at low effective normal stress conditions if the contacts are not broken but rather 'ride' past one another (top left and bottom left panels, Engelder and Scholz, 1976). At high effective normal stress, the transmissivity of the fracture is much lower than at low values. When shear displacement occurs at such high stresses, the contacts are sheared rather than simply displaced (Engelder and Scholz, 1976), this process results in a near constant (or decreased) transmissivity with increasing shear displacements. The production of gouge can also block hydraulic channels, as has been shown in this study. b. Depiction of the evolution of transmissivity with increasing displacement as measured in this study for all surface roughness configurations: when irreversible shear displacement occurs, transmissivity remains almost constant, as observed also by Rutter and Mecklenburgh (2018) in other rock lithologies.

5. CONCLUSIONS

We presented the results of Acosta et al. (2020) that developed an experimental technique to customize the surface roughness of real-rock samples which had a fully controlled geometry, precisely measured, and analyzed. The fractures were experimentally loaded under deep reservoir conditions (both under normal and shear loading) to study fluid flow through them.

We observed that the main controls on fluid flow through rough fractures are the surface geometry and the stress applied on the fracture (normal to the fracture plane). Regarding surface geometry, we observed that the imbrication of the main wavelengths, the h_{RMS}, and magnitude of the macroscopic wavelengths had a much larger influence on fluid flow than the Hurst exponent and the roll-off wave-vector of the power spectral density of heights. The application of normal stress significantly reduced fluid transport capacity compared to the application of shear stress. A numerical procedure could reproduce well hydraulic transport through rough fractures under normal stress by using a contact mechanics approach for the geometrical aperture distribution. Finally, small irreversible shear displacements (< 1mm) did not increase the fluid transport capacity of the rough fractures. For more details on experimental methods and results, the reader is referred to Acosta et al. (2020).

Further work is needed to develop a numerical procedure that allows simulating fractures under both normal and shear stresses. The target model should also include examination of shear induced plastic deformation and wear processes. This would allow coupling the evolution of fault roughness with the hydraulic transport properties as shear reactivation occurs. In addition, the issue of porosity unclogging in the fracture's core has been neglected in all this analysis. This should be the target of future experiments. Finally, the experiments of Acosta et al. (2020) were conducted in carbonate rocks, the flow channeling processes could be drastically different in silicates, reason why the conclusion should be re-evaluated in the light of experiments on silicates.

In the light of our results, during EGS stimulations, small shear displacements will not significantly increase the reservoir's permeability (unless porosity unclogging occurs). In turn, reducing the effective stress on the reservoir's fractures and faults will generate large permeability increases and improve the ability to predict its evolution. We discussed possible improvements on stimulation strategies for EGS reservoirs.

REFERENCES

Acosta, M., Violay, M. 2020, Mechanical and hydraulic transport properties of transverse-isotropic Gneiss deformed under deep reservoir stress and pressure conditions. *International journal of rock mechanics and mining sciences*.

Acosta, M., Maye, R., & Violay, M. (2020). Hydraulic transport through calcite bearing faults with customized roughness: effects of normal and shear loading. Journal of Geophysical Research: Solid Earth, 125(8), e2020JB019767.

Akchurin, A., Bosman, R., Lugt, P.M. and van Drogen, M., 2015. On a model for the prediction of the friction coefficient in mixed lubrication based on a load-sharing concept with measured surface roughness. *Tribology letters*, *59*(1), p.19.

Breede, K., Dzebisashvili, K., Liu, X. and Falcone, G., 2013. A systematic review of enhanced (or engineered) geothermal systems: past, present and future. *Geothermal Energy*, *1*(1), p.4.

Brown, S., Caprihan, A. and Hardy, R., 1998. Experimental observation of fluid flow channels in a single fracture. *Journal of Geophysical Research: Solid Earth*, *103*(B3), pp.5125-5132.

Brown, S.R. and Scholz, C.H., 1985. Broad bandwidth study of the topography of natural rock surfaces. *Journal of Geophysical Research: Solid Earth*, *90*(B14), pp.12575-12582.

Brown, S.R., 1987. A note on the description of surface roughness using fractal dimension. *Geophysical Research Letters*, *14*(11), pp.1095-1098.

Brown, S.R., 1987. Fluid flow through rock joints: the effect of surface roughness. *Journal of Geophysical Research: Solid Earth*, *92*(B2), pp.1337-1347.

Brush, D.J. and Thomson, N.R., 2003. Fluid flow in synthetic rough-walled fractures: Navier-Stokes, Stokes, and local cubic law simulations. *Water Resources Research*, *39*(4).

Candela, T., Renard, F., Bouchon, M., Brouste, A., Marsan, D., Schmittbuhl, J. and Voisin, C., 2009. Characterization of fault roughness at various scales: Implications of three-dimensional high resolution topography measurements. In *Mechanics, structure and evolution of fault zones* (pp. 1817-1851). Birkhäuser Basel.

Candela, T., Renard, F., Klinger, Y., Mair, K., Schmittbuhl, J. and Brodsky, E.E., 2012. Roughness of fault surfaces over nine decades of length scales. *Journal of Geophysical Research: Solid Earth*, *117*(B8).

Carey, J.W., Lei, Z., Rougier, E., Mori, H. and Viswanathan, H., 2015. Fracture-permeability behavior of shale. *Journal of unconventional oil and gas resources*, *11*, pp.27-43.

Chen, Z., Narayan, S.P., Yang, Z. and Rahman, S.S., 2000. An experimental investigation of hydraulic behaviour of fractures and joints in granitic rock. *International Journal of Rock Mechanics and Mining Sciences*, *37*(7), pp.1061-1071.

Ciardo, F. and Lecampion, B., 2019. Effect of dilatancy on the transition from aseismic to seismic slip due to fluid injection in a fault. *Journal of Geophysical Research: Solid Earth*, *124*(4), pp.3724-3743.

Cladouhos, T., Petty, S., Foulger, G., Julian, B. and Fehler, M., 2010. Injection induced seismicity and geothermal energy. *GRC Transactions*, *34*, pp.1213-1220.

Cornet, F.H., 2016. Seismic and aseismic motions generated by fluid injections. *Geomechanics for Energy and the Environment*, *5*, pp.42-54.

Crawford, B.R., Faulkner, D.R. and Rutter, E.H., 2008. Strength, porosity, and permeability development during hydrostatic and shear loading of synthetic quartz-clay fault gouge. *Journal of Geophysical Research: Solid Earth*, *113*(B3).

Delle Piane, C., Arena, A., Sarout, J., Esteban, L. and Cazes, E., 2015. Micro-crack enhanced permeability in tight rocks: An experimental and microstructural study. *Tectonophysics*, *665*, pp.149-156.

Elkhoury, J.E., Niemeijer, A., Brodsky, E.E. and Marone, C., 2011. Laboratory observations of permeability enhancement by fluid pressure oscillation of in situ fractured rock. *Journal of Geophysical Research: Solid Earth*, *116*(B2).

Engelder, J.T. and Scholz, C.H., 1976, May. The role of asperity indentation and ploughing in rock friction—II: Influence of relative hardness and normal load. In International Journal of Rock Mechanics and Mining Sciences & Geomechanics Abstracts (Vol. 13, No. 5, pp. 155-163). Pergamon.

Esaki, T., Du, S., Mitani, Y., Ikusada, K. and Jing, L., 1999. Development of a shear-flow test apparatus and determination of coupled properties for a single rock joint. *International Journal of Rock Mechanics and Mining Sciences*, *36*(5), pp.641-650.

Faoro, I., Niemeijer, A., Marone, C. and Elsworth, D., 2009. Influence of shear and deviatoric stress on the evolution of permeability in fractured rock. *Journal of Geophysical Research: Solid Earth*, *114*(B1).

Faulkner, D.R., Jackson, C.A.L., Lunn, R.J., Schlische, R.W., Shipton, Z.K., Wibberley, C.A.J. and Withjack, M.O., 2010. A review of recent developments concerning the structure, mechanics and fluid flow properties of fault zones. *Journal of Structural Geology*, *32*(11), pp.1557-1575.

Fryer, B., Siddiqi, G. and Laloui, L., 2020. Injection-induced seismicity: strategies for reducing risk using high stress path reservoirs and temperature-induced stress preconditioning. *Geophysical Journal International*, *220*(2), pp.1436-1446.

Grasselli, G. and Egger, P., 2003. Constitutive law for the shear strength of rock joints based on three-dimensional surface parameters. *International Journal of Rock Mechanics and Mining Sciences*, *40*(1), pp.25-40.

Grigoli, F., Cesca, S., Priolo, E., Rinaldi, A.P., Clinton, J.F., Stabile, T.A., Dost, B., Fernandez, M.G., Wiemer, S. and Dahm, T., 2017. Current challenges in monitoring, discrimination, and management of induced seismicity related to underground industrial activities: A European perspective. *Reviews of Geophysics*, *55*(2), pp.310-340.

Guo, T., Zhang, S., Gao, J., Zhang, J. and Yu, H., 2013. Experimental study of fracture permeability for stimulated reservoir volume (SRV) in shale formation. *Transport in porous media*, *98*(3), pp.525-542.

Hakami, E., 1989. *Water flow in single rock joints* (No. STRIPA-TR--89-08). Swedish Nuclear Fuel and Waste Management Co..

Ishibashi, T., Watanabe, N., Hirano, N., Okamoto, A. and Tsuchiya, N., 2012. Upgrading of aperture model based on surface geometry of natural fracture for evaluating channeling flow. *Geothermal Resources Council, Transactions*, *36*, pp.481-486.

Iwai, K., 1976. Fundamental studies of fluid flow through a single fracture. *Ph. D. thesis, Univ. of California*.

Jacobs, T.D., Junge, T. and Pastewka, L., 2017. Quantitative characterization of surface topography using spectral analysis. *Surface Topography: Metrology and Properties*, *5*(1), p.013001.

Ji, Y., Hofmann, H., Rutter, E. H., Xiao, F., & Yang, L. (2022). Revisiting the Evaluation of Hydraulic Transmissivity of Elliptical Rock Fractures in Triaxial Shear-Flow Experiments. *Rock Mechanics and Rock Engineering*, 1-9.

Kanafi, 2019. Radially averaged surface roughness/topography power spectrum (PSD) (https://www.mathworks.com/matlabcentral/fileexchange/54297-radially-averaged-surface-roughness-topography-power-spectrum-psd), MATLAB Central File Exchange. Retrieved February 23, 2019.

Kanafi (2018). Surface generator: artificial randomly rough surfaces (https://www.mathworks.com/matlabcentral/fileexchange/60817-surface-generator-artificial-randomly-rough-surfaces), MATLAB Central File Exchange. Retrieved February 23, 2018.

Kang, P.K., Brown, S. and Juanes, R., 2016. Emergence of anomalous transport in stressed rough fractures. *Earth and Planetary Science Letters*, *454*, pp.46-54.

Konzuk, J.S. and Kueper, B.H., 2004. Evaluation of cubic law based models describing single-phase flow through a rough-walled fracture. *Water Resources Research*, *40*(2).

Lee, H.S. and Cho, T.F., 2002. Hydraulic characteristics of rough fractures in linear flow under normal and shear load. *Rock Mechanics and Rock Engineering*, *35*(4), pp.299-318.

Lomize, G.M., 1951. Flow in fractured rocks. *Gosenergoizdat, Moscow*, *127*, p.197.

Lubrecht, A.A. and Ioannides, E., 1991. A fast solution of the dry contact problem and the associated sub-surface stress field, using multilevel techniques.

Doron M., Sagy A., Tal Y., Hatzor Y.H., 2022, Fault roughness controls sliding instability, *Earth and Planetary Science Letters*, Volume 579.

Olsson, W.A. and Brown, S.R., 1993, December. Hydromechanical response of a fracture undergoing compression and shear. In *International journal of rock mechanics and mining sciences and geomechanics abstracts* (Vol. 30, No. 7, pp. 845-851). Pergamon.

Orellana, L. F., Giorgetti, C., & Violay, M. (2019). Contrasting mechanical and hydraulic properties of wet and dry fault zones in a proposed shale-hosted nuclear waste repository. *Geophysical Research Letters*, *46*(3), 1357-1366.

Oron, A.P. and Berkowitz, B., 1998. Flow in rock fractures: The local cubic law assumption reexamined. *Water Resources Research*, *34*(11), pp.2811-2825.

Park, J.W. and Song, J.J., 2013. Numerical method for the determination of contact areas of a rock joint under normal and shear loads. *International Journal of Rock Mechanics and Mining Sciences*, *58*, pp.8-22.

Patir, N. and Cheng, H.S., 1978. An average flow model for determining effects of three-dimensional roughness on partial hydrodynamic lubrication.

Piggott, A.R. and Elsworth, D., 1992. Analytical models for flow through obstructed domains. *Journal of Geophysical Research: Solid Earth*, *97*(B2), pp.2085-2093.

Polonsky, I.A. and Keer, L.M., 1999. A numerical method for solving rough contact problems based on the multi-level multi-summation and conjugate gradient techniques. *Wear*, *231*(2), pp.206-219.

Power, W.L., Tullis, T.E., Brown, S.R., Boitnott, G.N. and Scholz, C.H., 1987. Roughness of natural fault surfaces. *Geophysical Research Letters*, *14*(1), pp.29-32.

Power, W.L. and Tullis, T.E., 1989. The relationship between slickenside surfaces in fine-grained quartz and the seismic cycle. *Journal of Structural Geology*, *11*(7), pp.879-893.

Pyrak-Nolte, L.J. and Morris, J.P., 2000. Single fractures under normal stress: The relation between fracture specific stiffness and fluid flow. *International Journal of Rock Mechanics and Mining Sciences*, *37*(1-2), pp.245-262.

Pyrak-Nolte, L.J., Cook, N.G. and Nolte, D.D., 1988. Fluid percolation through single fractures. *Geophysical Research Letters*, *15*(11), pp.1247-1250.

Renard, F., Candela, T. and Bouchaud, E., 2013. Constant dimensionality of fault roughness from the scale of micro-fractures to the scale of continents. *Geophysical Research Letters*, *40*(1), pp.83-87.

Renshaw, C.E., 1995. On the relationship between mechanical and hydraulic apertures in rough-walled fractures. *Journal of Geophysical Research: Solid Earth*, *100*(B12), pp.24629-24636.

Reynolds, Osborne. "IV. On the theory of lubrication and its application to Mr. Beauchamp tower's experiments, including an experimental determination of the viscosity of olive oil." *Philosophical transactions of the Royal Society of London* 177 (1886): 157-234.

Rutter, E.H. and Mecklenburgh, J., 2017. Hydraulic conductivity of bedding-parallel cracks in shale as a function of shear and normal stress. *Geological Society, London, Special Publications*, *454*(1), pp.67-84.

Rutter, E.H. and Mecklenburgh, J., 2018. Influence of normal and shear stress on the hydraulic transmissivity of thin cracks in a tight quartz sandstone, a granite, and a shale. *Journal of Geophysical Research: Solid Earth*, *123*(2), pp.1262-1285.

Sagy, A., Brodsky, E.E. and Axen, G.J., 2007. Evolution of fault-surface roughness with slip. *Geology*, *35*(3), pp.283-286.

Sahli, R., Pallares, G., Ducottet, C., Ali, I.B., Al Akhrass, S., Guibert, M. and Scheibert, J., 2018. Evolution of real contact area under shear and the value of static friction of soft materials. *Proceedings of the National Academy of Sciences*, *115*(3), pp.471-476.

Sawayama, K., Ishibashi, T., Jiang, F., Tsuji, T., & Fujimitsu, Y. (2021). Relating Hydraulic–Electrical–Elastic Properties of Natural Rock Fractures at Elevated Stress and Associated Transient Changes of Fracture Flow. *Rock Mechanics and Rock Engineering*, *54*(5), 2145-2164.

Shvarts, A., 2019. *Coupling mechanical frictional contact with interfacial fluid flow at small and large scales* (Doctoral dissertation).

Shvarts, A.G. and Yastrebov, V.A., 2018a. Trapped fluid in contact interface. *Journal of the Mechanics and Physics of Solids*, *119*, pp.140-162.

Shvarts, A.G. and Yastrebov, V.A., 2018b. Fluid flow across a wavy channel brought in contact. *Tribology International*, *126*, pp.116-126.

Sibson, R.H., 1994. Crustal stress, faulting and fluid flow. *Geological Society, London, Special Publications*, *78*(1), pp.69-84.

Sibson, R.H., 1996. Structural permeability of fluid-driven fault-fracture meshes. *Journal of Structural Geology*, *18*(8), pp.1031-1042.

Spijker, P., Anciaux, G. and Molinari, J.F., 2013. Relations between roughness, temperature and dry sliding friction at the atomic scale. *Tribology International*, *59*, pp.222-229.

Tanikawa, W., Sakaguchi, M., Tadai, O. and Hirose, T., 2010. Influence of fault slip rate on shear-induced permeability. *Journal of Geophysical Research: Solid Earth*, *115*(B7).

Tesei, T., Carpenter, B. M., Giorgetti, C., Scuderi, M. M., Sagy, A., Scarlato, P., & Collettini, C. (2017). Friction and scale-dependent deformation processes of large experimental carbonate faults. *Journal of Structural Geology*, *100*, 12–23.

Townend, J. and Zoback, M.D., 2000. How faulting keeps the crust strong. *Geology*, *28*(5), pp.399-402.

Tribonet: https://www.tribonet.org/cmdownloads/tribology-simulator/

Violay, M., Nielsen, S., Gibert, B., Spagnuolo, E., Cavallo, A., Azais, P., Vinciguerra, S. and Di Toro, G., 2014. Effect of water on the frictional behavior of cohesive rocks during earthquakes. *Geology*, *42*(1), pp.27-30.

Walsh, J.B. and Brace, W.F., 1984. The effect of pressure on porosity and the transport properties of rock. *Journal of Geophysical Research: Solid Earth*, *89*(B11), pp.9425-9431.

Walsh, J.B., 1981, Effect of pore pressure and confining pressure on fracture permeability. In *International Journal of Rock Mechanics and Mining Sciences and Geomechanics Abstracts* (Vol. 18, No. 5, pp. 429-435). Pergamon.

Watanabe, N., Hirano, N. and Tsuchiya, N., 2008. Determination of aperture structure and fluid flow in a rock fracture by high-resolution numerical modeling on the basis of a flow-through experiment under confining pressure. *Water Resources Research*, *44*(6).

Watanabe, N., Hirano, N. and Tsuchiya, N., 2009. Diversity of channeling flow in heterogeneous aperture distribution inferred from integrated experimental-numerical analysis on flow through shear fracture in granite. *Journal of Geophysical Research: Solid Earth*, *114*(B4).

Wenning, Q.C., Madonna, C., Kurotori, T. and Pini, R., 2019. Spatial mapping of fracture aperture changes with shear displacement using X-ray computerized tomography.

Witherspoon, P.A., Wang, J.S., Iwai, K. and Gale, J.E., 1980. Validity of cubic law for fluid flow in a deformable rock fracture. *Water resources research*, *16*(6), pp.1016-1024.

Yastrebov, V.A., Anciaux, G. and Molinari, J.F., 2017. The role of the roughness spectral breadth in elastic contact of rough surfaces. *Journal of the Mechanics and Physics of Solids*, *107*, pp.469-493.

Yeck, W.L., Weingarten, M., Benz, H.M., McNamara, D.E., Bergman, E.A., Herrmann, R.B., Rubinstein, J.L. and Earle, P.S., 2016. Far-field pressurization likely caused one of the largest injection induced earthquakes by reactivating a large preexisting basement fault structure. *Geophysical Research Letters*, *43*(19), pp.10-198.

Yeo, I.W., De Freitas, M.H. and Zimmerman, R.W., 1998. Effect of shear displacement on the aperture and permeability of a rock fracture. *International Journal of Rock Mechanics and Mining Sciences*, *35*(8), pp.1051-1070.

Zimmerman, R.W. and Bodvarsson, G.S., 1996. Hydraulic conductivity of rock fractures. *Transport in porous media*, *23*(1), pp.1-30.

Zoback, Mark D., and Steven M. Gorelick. "Earthquake triggering and large-scale geologic storage of carbon dioxide." *Proceedings of the National Academy of Sciences* 109, no. 26 (2012): 10164-10168.